A new route for preparing nanoporous Cu–Zn–Ni–Co alloy by electrodeposition and dealloying: Application as electrocatalysts for water reduction

Yuelin Xie, Antoine Miche, Vincent Vivier, Mireille Turmine

International Journal of Hydrogen Energy 127 (2025) 95–106

Contents lists available at ScienceDirect

International Journal of Hydrogen Energy

journal homepage: www.elsevier.com/locate/he

A new route for preparing nanoporous Cu–Zn–Ni–Co alloy by electrodeposition and dealloying: Application as electrocatalysts for water reduction

Yuelin Xie, Antoine Miche, Vincent Vivier, Mireille Turmine *

Sorbonne Université, CNRS, Laboratoire de Réactivité de Surface (LRS), 4 Place Jussieu, F-75005, Paris, France

ARTICLE INFO

Keywords:
Nanoporous of material electroplating
Ionic liquids
Deep eutectic solvents
Multielement electrodeposition
Hydrogen evolution reaction
Dealloying

ABSTRACT

Nanoporous Cu–Zn–Ni–Co alloys have been prepared on Cu foils by a two-step electrodeposition mechanism in ethylammonium nitrate (EAN), a protic ionic liquid, and ethaline, a deep eutectic solvent (DES). A porous alloy was then produced using a dealloying step. The physicochemical properties of ethaline containing Ni^{2+}, Co^{2+}, and Zn^{2+} salts were firstly investigated. The two-step electrodeposition process for the preparation and dealloying of Cu–Zn–Ni–Co alloys was then discussed. In the first step, cobalt was deposited on copper in pure EAN. Zinc and nickel were subsequently co-electrodeposited in ethaline to produce a Cu–Zn–Ni–Co alloy after further heat treatment. Nanoporous alloys were prepared by electrochemical and chemical dealloying to obtain different electrocatalytic properties for the hydrogen evolution reaction (HER). In comparison to the initial non-porous alloy, the HER performance has been markedly enhanced, with an HER potential reaching as low as −0.067 V/RHE. The novel approach of preparing nanoporous Cu–Zn–Ni–Co alloys by electrodeposition in ionic media, followed by dealloying, represents an efficient methodology for practical applications in electrocatalysis, including water splitting.

1. Introduction

Hydrogen is attracting increasing interest as a clean energy with high energy density and low emissions. As one of the simplest energy carriers, hydrogen (H_2) has demonstrated a remarkable ability to store energy, with a free energy value of 4.92 eV of free energy for the chemical bond [1]. Water electrolysis, also known as water splitting, is recognized as a promising approach to hydrogen production, providing the green hydrogen which is expected to dominate hydrogen production [2]. The hydrogen produced by water electrolysis is of high purity, and the process itself is safe and straightforward. For the hydrogen evolution reaction (HER) and oxygen evolution reaction (OER), the electrode material is one of the keys to the water electrolysis. In recent years, the research on the preparation of electrocatalysts has attracted increasing interest and more effective catalysts have been studied. Although precious metals have excellent properties for water splitting, their low natural reserves and high prices make their large-scale use avoidable. Therefore, the preparation of highly efficient transition metal alloy-based electrocatalysts for HER has been a hot research topic in recent years [3–5].

Adjusting the electronic structure of transition metal-based materials by alloying is one of the approaches being considered. Since the first investigations of the HER mechanism in metallic Ni–Co in the 1960s, extensive research has been devoted to the preparation and application of transition metal alloys [6,7]. Based on metallic Ni–Co, different alloys were studied as the electrocatalyst in HER. The NiCo(CrV) films were studied in the alkaline cell and the acidic cell with the overpotential of 87 mV and 50 mV in HER, respectively [8,9]. Various combinations of metal elements have been investigated in previous work [4,10–20]. For example, Shetty et al. prepared Ni–Mo alloys by electrodeposition. By adjusting the electrodeposition current, the ratio of Ni and Mo can be tuned. It has been shown that the different combination of elements by alloying can enhance the HER properties and the overpotential of HER decreased to −1.28 V with the addition of Mo [21].

In addition, the specific surface area of the electrocatalyst is a significant factor affecting the efficiency of the electrocatalytic process. In recent years, there has been a great deal of interest in the use of nanoporous alloys as electrocatalysts for water splitting. Nanoporous alloys have a high specific surface area due to the average number of holes distributed over the surface, and thus have great potential for catalytic

* Corresponding author.
E-mail address: mireille.turmine@sorbonne-universite.fr (M. Turmine).

https://doi.org/10.1016/j.ijhydene.2025.04.067
Received 8 December 2024; Received in revised form 26 March 2025; Accepted 3 April 2025

applications. One of the most common ways to prepare nanoporous alloys is dealloying, including chemical dealloying and electrochemical dealloying. Elements can be selectively oxidized and dissolved due to their potential difference, and the remaining elements on the surface can be rebuilt by diffusion. During the dealloying process, the free atoms form a new structure on the surface, which changes the surface element distribution and morphology [22,23]. This rearrangement of atoms helps to create the nanoporous structure. Chemical dealloying involves immersing alloys in a solvent, usually an acid or base solution, during which, the selected elements dissolve according to different parameters such as pH, time, and temperature. By dealloying the precursor, an amorphous Ag–Mg-Ga alloy, in HCl solution, Li et al. prepared nanoporous Ag [24]. First, the rapid dissolution of Mg and Ca atoms from the matrix in an HCl solution leads to the formation of surface vacancies. Then, Ag atoms accumulate at the interface to form an Ag nanocluster, which leads to a decrease in the surface energy. In contrast to chemical dealloying, the electrochemical dealloying process can be controlled by current or potential, while the morphologies and electrocatalytic properties can be tuned by adjusting the settings of the electrochemical dealloying.

Despite the intense interest in nanoporous alloys as electrocatalysts for water splitting, the literature shows that the morphologies and structures of these materials depend on a number of variables, including temperature, time, matrix composition, alloy composition, and the potential (for electrochemical dealloying) of the dealloying process. As a result, an increasing number of studies are being performed on these materials.

In this study, a two-step electrodeposition process for the preparation of Cu–Zn–Ni–Co alloys is reported. The process involves heat treatment after electrodeposition of the metals in ethylammonium nitrate (EAN) and ethaline solution, respectively. The resulting alloy, $Zn_{70.9}Ni_{12.7}Cu_{11.2}Co_{5.2}$, shows a continuously changing distribution of the elements from the substrate to the surface with different alloy phases. The aforementioned alloy has been used in the synthesis of nanoporous alloys using both chemical and electrochemical dealloying techniques. This strategy results in various morphologies, along with different elemental compositions and distributions within the nanoporous structures. Furthermore, the HER performance of these nanoporous alloys can be clarified by studying the different combinations of morphology and elemental constituents.

2. Experimental details

2.1. Chemicals and materials

Ethylamine ($CH_3CH_2NH_2$, 70 wt % in water, Acros Organics), nitric acid (HNO_3, 68 wt % in water, AnalaR NORMAPUR), potassium chloride (KCl, 99 %, Acros Organics), choline chloride (ChCl, Acros Organics, purity ≥99 %), ethylene glycol (EG, VWR Chemical, purity ≥99 %), potassium hydroxide (KOH, 86 %, Fisher Scientific), zinc chloride ($ZnCl_2$, 98 % purity, Sigma-Aldrich), cobalt chloride ($CoCl_2$, 98 % purity, Sigma-Aldrich), and nickel chloride ($NiCl_2$, 98 %, Sigma-Aldrich) were used as received.

Cu foils (purity 99.9 %, 0.5 cm^2 × 0.2 mm thickness, Qiaona, China) were used as the substrate for electroplating after washing in acetone and HNO_3, for 10 min, respectively, and polished with 2400 grit sandpaper before electrodeposition to obtain a smooth and clean surface. Nickel wire (purity >99 %, 1 mm diameter) was purchased from Chempur (Germany), cobalt wire (purity >99.99 %, 1 mm diameter) and zinc wire (purity >99.99 %, 0.3 mm diameter) were purchased from Chengshuo (China), and silver wire (purity 99.99 %) was purchased from Mateck (Germany).

2.2. Synthesis of the ionic liquid and the deep eutectic solvent

The ionic liquid, ethylammonium nitrate (EAN), was prepared by mixing concentrated aqueous solutions of ethylamine and nitric acid in a 1:1 molar ratio. The nitric acid solution was added dropwise to the aqueous ethylamine solution under stirring at a controlled temperature (T = 263 K). The purification of EAN was then performed by lyophilization (Freeze Dryer - 86 °C, OPERON CO., LTD.), which allowed to reduce the water content below 100 ppm (*vide infra*). The water content in freshly prepared solvent was titrated using a Karl Fisher coulometer (C20, Mettler Toledo) in a glove-box (Concept GP, Jacomex). Ethaline was prepared by mixing choline chloride and ethylene glycol in a molar ratio of 1:2. The mixture was stirred at a temperature of 60 °C for 3 h to obtain a homogeneous and transparent liquid. The salts used for electrochemistry were dried by both heating and lyophilization in order to reduce the amount of water in the electrolytes. Solutions of different salts ($NiCl_2$, $CoCl_2$, $ZnCl_2$ and their mixtures) in EAN and ethaline were prepared by mixing the different compounds with stirring at 333 K for 24 h after weighing. The density and viscosity of the solutions were measured using a densimeter (DSA 5000 M, Anton Paar) and a microviscometer (Lovis 2000 M, Anton Paar), respectively. The conductivity and pH values of the solutions were measured with a conductivity meter (CDM230, Radiometer Analytical) and a pH meter (PHM250, Radiometer Analytical), respectively.

2.3. Electrodeposition

All electrochemical measurements and electrodepositions were performed using a three-electrode cell and a GAMRY REF600+ potentiostat. The Cu foils were used as working electrodes after the polishing and cleaning steps. The reference electrode consisted of a double junction compartment, in which a silver wire was immersed in the first compartment containing a saturated EAN or ethaline solution of silver nitrate ($AgNO_3$), with a sintered glass at the bottom. The second compartment was jacketed from the first junction with pure EAN or ethaline in order to prevent the ion diffusion from the reference to the electrolyte. A 15 mm in diameter nickel, cobalt, and zinc rings were used as the counter electrodes for the electrodeposition processes, corresponding to Ni, Co, and Zn based deposition preparations, respectively. Argon was bubbled into the electrolyte for 15 min prior to electrochemical measurements. All electroplating alloys prepared in EAN were performed within a glove box to avoid oxygen contamination and to limit water ingress.

2.4. Heat treatment and dealloying

In the two-step electrodeposition process, the cobalt was first deposited on the copper foil in EAN. Subsequently, sample is heat treated to form the Cu–Co alloy. Prior to the heating step, a continuous flow of argon gas was introduced for 2 h to create an inert atmosphere. Then, the temperature inside the tube furnace was raised from room temperature to 400 °C at a rate of 3 °C/min and maintained at this temperature for 10 min to obtain a homogeneous alloy. Then, the sample was gradually cooled to room temperature in the furnace, while maintaining the argon gas flow to prevent any exposure to atmospheric air throughout the process. Then, Zn–Ni alloys were electrodeposited on the surface of Cu–Co alloys in ethaline. A second heat treatment, with the same heat treatment parameters, produced Zn–Ni–Cu–Co alloys. In a final step, the porous alloys were prepared by chemical dealloying or electrochemical dealloying in CH_3COOH, HNO_3, KOH, H_3PO_4, respectively. These different solutions were selected due to their varying strengths, in order to learn the relationship between the electrocatalyst morphology and the dealloying parameters.

2.5. Characterizations

The crystal structures of the electrodeposited materials were obtained by X-ray diffraction (XRD, D8 ADVANCE BRUKER) at a scan rate of $5^\circ \cdot min^{-1}$ from 20° to 80° using the Cu K_α radiation. The surface

morphologies of the electrodeposits were observed by scanning electron microscopy (SEM, SU-70 HITACHI) using a voltage of 5 kV and by energy dispersive X-ray spectroscopy at a voltage of 15 kV (EDS, Ultim Max, Oxford Instruments). XPS analyses were performed using an Omicron Argus X-ray photoelectron spectrometer, equipped with a monochromated AlKα radiation source ($h\nu = 1486.6$ eV) and a 280 W electron beam power. The emission of photoelectrons from the sample was analyzed at a photoelectron collection angle of 45° under ultra-high vacuum conditions ($\leq 10^{-9}$ mBar). Spectra were carried out with a 100 eV pass energy for the survey scan and 20 eV pass energy for core levels regions. Binding energies were referenced to the C 1s peak due to carbon bound to only carbon and hydrogen at 284.8 eV and element peak intensities were corrected by Scofield factors. The peak areas were determined after subtraction of a U 2 Tougaard background. The spectra were fitted using Casa XPS software (Casa Software Ltd, U.K.) and applying a gaussian/lorentzian ratio g/l equal to 70/30 for deconvolution.

2.6. Hydrogen evolution reaction

A three-electrode cell was also used for all the electrocatalysis experiments. The alloy deposit was used as the working electrode, and a platinum mesh electrode and a Hg/HgO electrode were used as the counter and reference electrodes, respectively. The electrolyte temperature was controlled at 25.0 ± 0.1 °C with a thermostatic bath. A 1.0 M KOH solution was used as the electrolyte. Argon was bubbled into the electrolyte for 15 min prior to each experiment, and an argon flow was maintained over the cell for the duration of the measurement.

The effective active surface area (ECSA) of the samples was evaluated by measuring the interfacial capacitance (C^{σ}) [25].

To facilitate comparison of our results for water splitting, all potentials were converted with respect to the reversible hydrogen electrode (RHE) using the following relationship:

$$E\,(vs.\ \mathrm{RHE}) = E\,(vs.\ \mathrm{Hg/HgO}) + 0.059\ \mathrm{pH} + 0.095 \quad (1)$$

3. Results and discussion

3.1. Physicochemical properties of ethaline electrolytes

Table 1 provides an overview of the physicochemical properties of various electrolytes used in this study, namely viscosity, density, pH, and conductivity, as a function of the temperature. As shown in Fig. S1 (Supporting Information), an increase in temperature leads to a decrease in density, viscosity, and pH, while conductivity increases. This phenomenon is observed for electrolyte solutions with different ion concentrations. It is noteworthy that the addition of $CoCl_2$, $NiCl_2$, and $ZnCl_2$ to ethaline results in a slight increase in density, which can be attributed to the slight swelling of ethaline at the same temperature. In addition, an increase in temperature results in a decrease in the viscosity of the solutions. To illustrate this behavior, note that the viscosity of the ethaline solution increases from 43.68 to 110.90 mPa s when 0.5 M of $NiCl_2$ is added at 25 °C. Similarly, solutions containing $NiCl_2$ show a higher viscosity than that of pure ethaline. In contrast, the incorporation of $ZnCl_2$ and $CoCl_2$ was observed to have a slight reducing effect on for the viscosity of ethaline. In fact, at 25 °C the viscosity of ethaline with 0.5 M $CoCl_2$ and 0.5 M $ZnCl_2$ is 39.17 mPa s and 36.05 mPa s, respectively. At 25 °C, the conductivities of all ethaline solutions are similar, with values close to that of pure ethaline (7.97 mS cm^{-1}). However, notable exceptions are observed in ethaline with 0.5 M $NiCl_2$ and with 0.5 M $NiCl_2$ + 0.25 M $ZnCl_2$, which have conductivities of 4.02 mS cm^{-1} and 4.43 mS cm^{-1}, respectively. The pH of pure ethaline at 25 °C is 4.18. Ethaline solutions containing metal salts have a higher pH than pure ethaline, with the exception of solutions containing 0.5 M $CoCl_2$. There is currently no known pH measurement for $CoCl_2$ solutions. The reaction of Co^{2+} and water in an ethaline solution results in the formation of H^+ and CoO. The subsequent reaction of CoO and water produces more H^+, which lowers the pH value [26]. The conductivity is markedly higher and the viscosity is considerably smaller for the higher temperatures. Although Ni electrodeposition can be performed at room temperature, a higher electrodeposition efficiency can be achieved by performing electrodeposition at temperature above 60 °C.

3.2. Preparation of nanoporous Cu–Zn–Ni–Co alloys

In the two-step electrodeposition process, Co was initially deposited on Cu foil for 1 h in a glove box, following the parameters from our previous study for the electrodeposition of only two metals [27]. The potential was set at −1.05 V/Ag/Ag^+, based on the LSV curves presented in Fig. 1a. From the chronoamperometry presented in Fig. 1b, the calculated yield of cobalt on Cu foil is 1.14×10^{-4} mol. The cobalt deposit was then heated to 400 °C for 30 min, forming a Co–Cu alloy.

Table 1
Physicochemical properties of the solutions used in this work.

Concentration	Temperature (°C)	Density (g·cm^{-3})	Viscosity (mPa·s)	Conductivity (mS·cm^{-1})	pH
Ethaline	25	1.116403	43.68	7.97	4.18
	40	1.107858	24.92	9.77	4.02
	60	1.096607	13.63	15.32	3.80
	80	1.085478	9.15	21.34	3.65
0.5 M $NiCl_2$	25	1.162129	110.90	4.02	5.35
	40	1.153427	55.52	6.77	5.15
	60	1.141552	25.67	10.35	5.05
	80	1.128869	13.39	13.60	4.75
0.5 M $CoCl_2$	25	1.147278	39.17	8.60	–
	40	1.138522	22.47	12.44	–
	60	1.126946	12.45	16.57	–
	80	1.115439	7.93	22.89	–
0.5 M $ZnCl_2$	25	1.150352	36.05	8.33	7.76
	40	1.141558	20.68	11.93	7.45
	60	1.129912	11.52	16.56	7.02
	80	1.118317	7.88	23.30	6.67
0.5 M $NiCl_2$ + 0.25 M $ZnCl_2$	25	1.181785	89.50	4.43	5.52
	40	1.173079	45.95	6.97	5.42
	60	1.161475	22.36	10.96	5.22
	80	1.149488	12.36	14.26	5.00
0.15 M $NiCl_2$ + 0.35 M $ZnCl_2$	25	1.167740	64.61	8.12	5.68
	40	1.159040	35.08	11.54	5.49
	60	1.147544	18.26	13.67	5.40
	80	1.135996	10.85	17.34	5.29

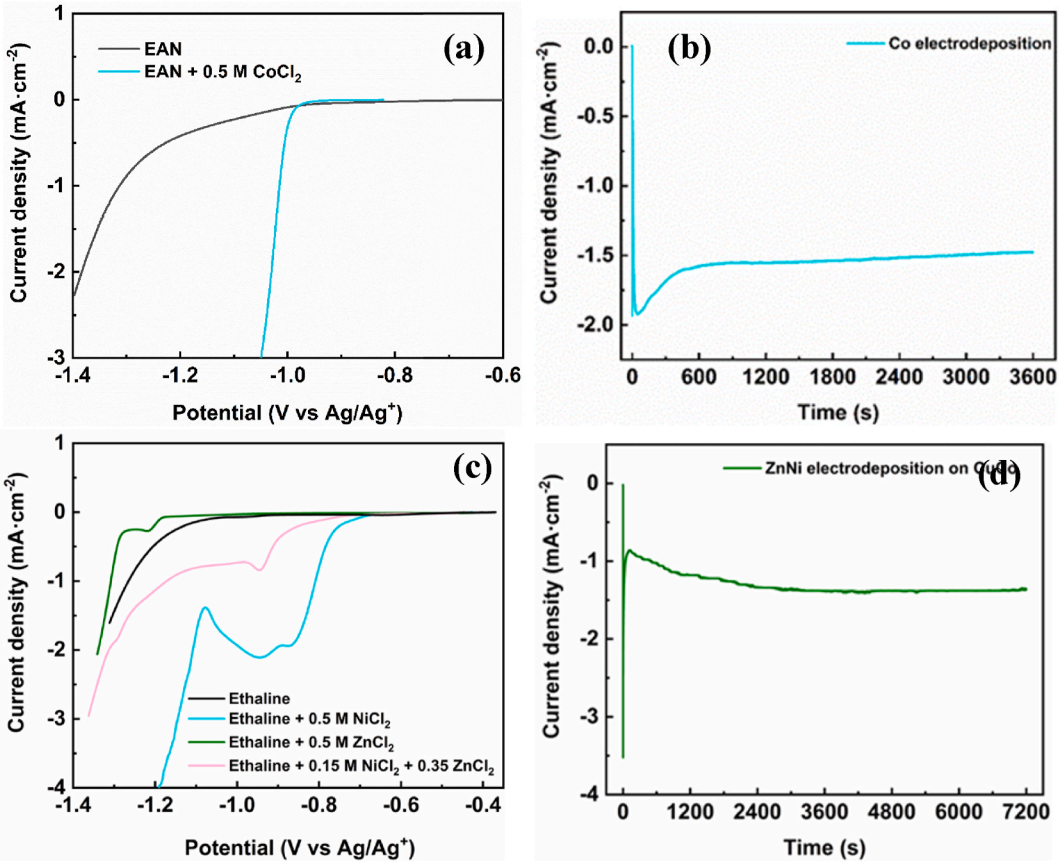

Fig. 1. a) Linear sweep voltammetry (LSV) curves of 0.5 M $CoCl_2$ in EAN on Cu foil at 60 °C in a glove box, b) Chronoamperometry for Co electrodeposition, c) LSV curves of ethaline with $NiCl_2$/$ZnCl_2$ on Co–Cu substrate at 40 °C, d) Chronoamperometry for Zn–Ni electrodeposition on Co–Cu.

Fig. 1c illustrates the electrochemical behavior of the Co–Cu alloy, which is now used as an electrode for performing the deposit of Zn and Ni from ethaline solutions containing 0.35 M $ZnCl_2$ and 0.15 M $NiCl_2$. The Co–Cu alloy reduces ethaline at −1.08 V/Ag/Ag^+. The reduction reaction of Ni^{2+} occurs in the electrochemical window of ethaline, between −0.68 V/Ag/Ag^+ and −1.08 V/Ag/Ag^+. The reduction reaction of Zn^{2+} occurs within the potential range of −1.25 to −1.31 V/Ag/Ag^+, which extends beyond the limits of the ethaline electrochemical window in the cathodic scan. The Zn–Ni deposition process was performed at −1.3 V/Ag/Ag^+ for 2 h, and the resulting chronoamperometry for this deposit step is presented in Fig. 1d. The 2-h electrodeposition process yielded a total charge transfer of 25.5 C, resulting in the deposition of 1.32×10^{-4} mol of Zn–Ni alloy on the Co–Cu substrate. The deposited sample was then heated (using the same parameters than for the Co–Cu alloy) to obtain the Cu–Zn–Ni–Co alloy.

The dealloying parameters related to the electrochemical dissolution of each element and alloy were ascertained through a cyclic voltammetry (CV) analysis, as illustrated in Fig. 2. It is important to evaluate the oxidation potentials of the different alloying elements in order to select the most suitable oxidation potential for the electrochemical dealloying process. The CV curve of a Cu foil in 1 M KOH (Fig. 2a) shows distinct oxidation peaks at 0.75 V/RHE, 1.0 V/RHE, and 1.16 V/RHE, thereby indicating that the oxidation potential range for Cu extends from 0.65 to 1.2 V/RHE. This observation is consistent with previous results regarding the oxidation behavior of copper [28]. Fig. 2b shows the CV curve for nickel. The oxidation peak at 1.62 V/RHE is attributed to the oxidation of Ni into Ni^{2+} and $Ni(OH)_2$/NiOOH, which is consistent with the literature [29,30]. The two peaks observed during the cathodic scan can be attributed to the reduction of Ni^{2+}. The CV curve of cobalt is presented in Fig. 2c. During the anodic scan, an oxidation peak corresponding to the oxidation of Co is observed within the potential range of 1.2–1.35 V/RHE. Similar to the case of Ni, the reduction of cobalt species is observed during the cathodic scan. The direct measurement of the electrochemical behavior of zinc in 1 M KOH is challenging due to the rapid and spontaneous dissolution of the metal in the alkaline solution. However, based on data obtained from previous work, it can be postulated that the reduction potential of zinc is lower than that of copper in an alkaline environment [31,32].

The CV curves of the Cu–Zn–Ni–Co alloys were analyzed on the basis of the CV curves measured for each individual element to gain insight into the origin of the different peaks observed. As shown in Fig. 2d, the CV curve for the Cu–Zn–Ni–Co alloy deposited in a two-step process exhibits several discernible peaks. At 0.26 V/RHE, a small peak can be attributed to the dissolution of zinc. It is followed by broad peaks at 0.75 V/RHE, and between 0.95 and 1.24 V/RHE, which can be attributed to copper oxidation. Two peaks at 1.35 and 1.5 V/RHE can be attributed to nickel oxidation. Previous studies have shown that the peaks associated with nickel oxidation can be attributed to a number of different processes, including the oxidation of Ni to Ni^+, and the subsequent oxidation of Ni^+ to Ni^{2+}. These peaks may also be the result from the oxidation of nickel to NiOOH or $Ni(OH)_2$, followed by further oxidation [33]. It is challenging to identify cobalt dissolution in the alloy's CV since it is generally weak and readily masked by other peaks. In addition, the current values associated with the reduction peaks of copper and nickel show a significant increase after the first scan. This is mainly due to the peeling of the surface oxide layer and the dissolution of zinc after the first redox scan. The presence of more copper, cobalt, and nickel in the deposited layer is confirmed by subsequent EDS analysis, which corroborates the existence of a gradient distribution of these elements beneath the surface. A more detailed examination of this phenomenon will be provided in the following section. Furthermore, the irreversible transformation of α-$Ni(OH)_2$ to β-$Ni(OH)_2$ results in the

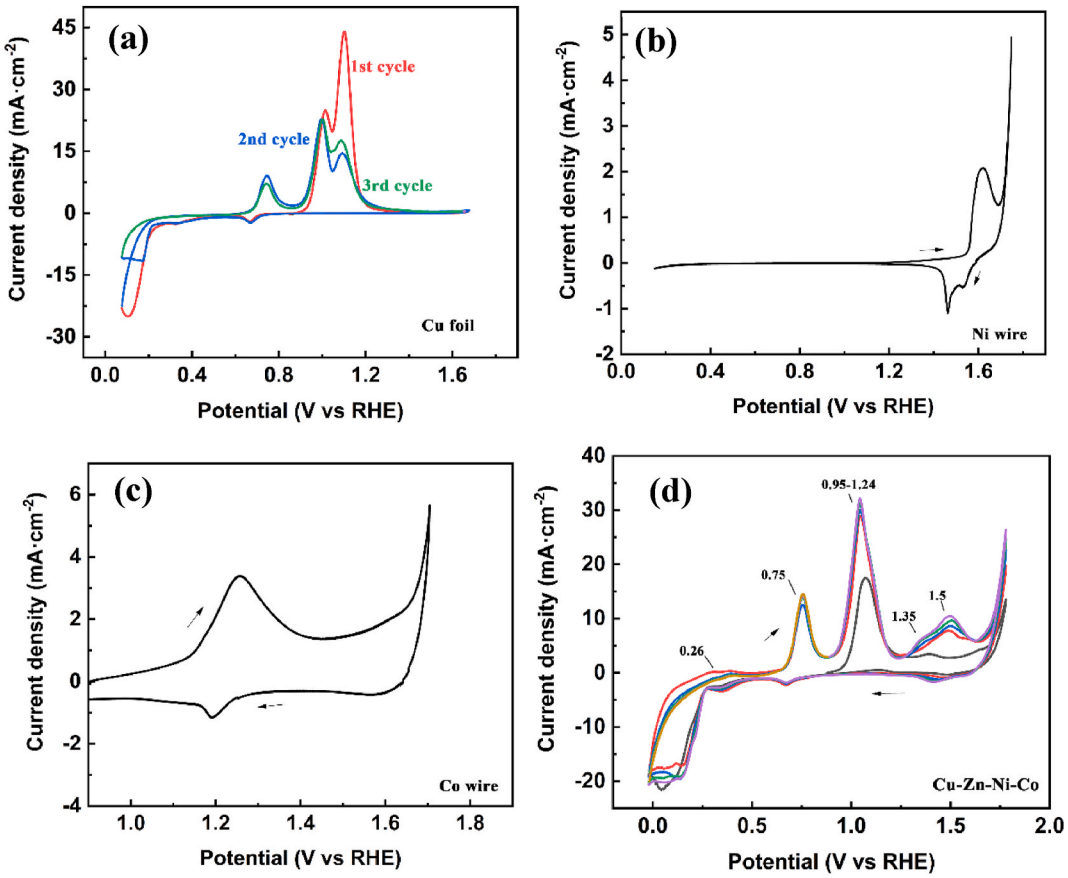

Fig. 2. CV curves of Cu foil (a), Ni wire (b), Co wire (c), and two-step deposited Cu–Zn–Ni–Co alloy (d) in 1 M KOH at 40 °C.

accumulation of the latter on the surface after the initial cycle. This phenomenon contributes to the observed increase in current during the subsequent oxidation of $Ni(OH)_2$/NiOOH [34]. In light of this discussion, the parameters of dealloying for each deposited Cu–Zn–Ni–Co alloy in KOH, HNO_3 and H_3PO_4 have been subjected to further investigation, and the results are presented in Table S1.

Fig. 3 shows the XRD patterns of the alloys at various stages of preparation. In the case of the two-step electrodeposition, the peaks observed subsequent to the initial are exclusively those of Cu (Fig. 3a). This is because there is less Co and more Cu from the substrate. Following the heat treatment, Co has occurred, resulting in the appearance of a peak attributed to CoO (Fig. 3b). Moreover, additional peaks corresponding to $CuCoN_{0.6}$ are observed at 42°, 49°, and 72°. These results are in agreement with our previous work, which demonstrated that the electrodeposition of Co in EAN is accompanied by a relatively low residual nitrogen content from the electrolyte. The residual nitrogen contributes to the formation of the new phase through diffusion during the subsequent heat treatment process [27]. Following the deposition of the Zn–Ni alloy during the second step, the XRD pattern presented in Fig. 3c shows only discrete diffraction peaks of Cu, which originate from the matrix material. Following the heat treatment, the XRD pattern shows the emergence of intricate phases, as illustrated in Fig. 3d. Apart from a small amount of unoxidized Zn, it is evident that the diffraction peaks predominantly originate from the diffusion of Cu to form new solid solutions or intermetallic compounds, such as $Cu_{3.8}Ni$ and Cu_5Zn_8. This indicates that the formation of alloy phases through the diffusion of Cu and Co from the low layer after the heat treatment is a viable approach for the preparation of multi-element materials. Furthermore, a minor amount of ZnO is present, indicating the oxidation of Zn during the heat treatment process. All phases are identified through the database code shown in the supporting information.

The morphology and the elemental distribution of the prepared alloys were analyzed by scanning electron microscopy (SEM) and energy-dispersive X-ray spectroscopy (EDS), as shown in Fig. 4. After 1 h, the Co electrodeposited has visible grains, as shown in Fig. 4a. After heating for 30 min, the sample exhibits a more compact grain structure (Fig. 4b). The 2-h Zn–Ni electrodeposit presented in Fig. 4c, has a similar grain structure, suggesting that the deposition and growth process continues along the Co–Cu alloy after heat treatment, resulting in a more compact structure after the second heat treatment.

It can be observed that the surface of the alloy remains consistently flat both prior to and after the heat treatment. As a result, it is difficult to determine whether a process of element diffusion has occurred. However, when the EDS and XRD results are considered together, it becomes apparent that there have been changes in the distribution of elements and structures on the alloy. This is demonstrated in Fig. S2, wherein the EDS spectra show discernible signals for Cu in all samples, accompanied by variable oxygen content. Table 2 shows the corresponding element contents. After 1 h of cobalt electrodeposition, a higher amount of Co is on Cu, reaching 61.7 at%. After the heat treatment, the Co content decreased to 50.6 at%, while the Cu content increased from 25.8 to 35.5 at%. This is due to Cu diffusing from the base to the surface and Co diffusing from the surface to the inner layer of Cu. The oxygen content increased from 12.5 to 13.8 at%, forming cobalt oxides, as confirmed by XRD analysis. In the case of the Zn–Ni alloy deposited in ethaline, zinc is the main element, reaching a content of 68.1 at%. After the heat treatment, the oxygen content increased significantly from 10.3 to 22.4 at% due to the formation of oxides, corresponding to the ZnO phase identified in the XRD results. Furthermore, following the application of heat treatment, the content of Zn, Ni, and Co within the alloy components decreased, while that of Cu increased. This phenomenon can be attributed to the diffusion of Co, Zn, and Ni into the alloy layer and also the

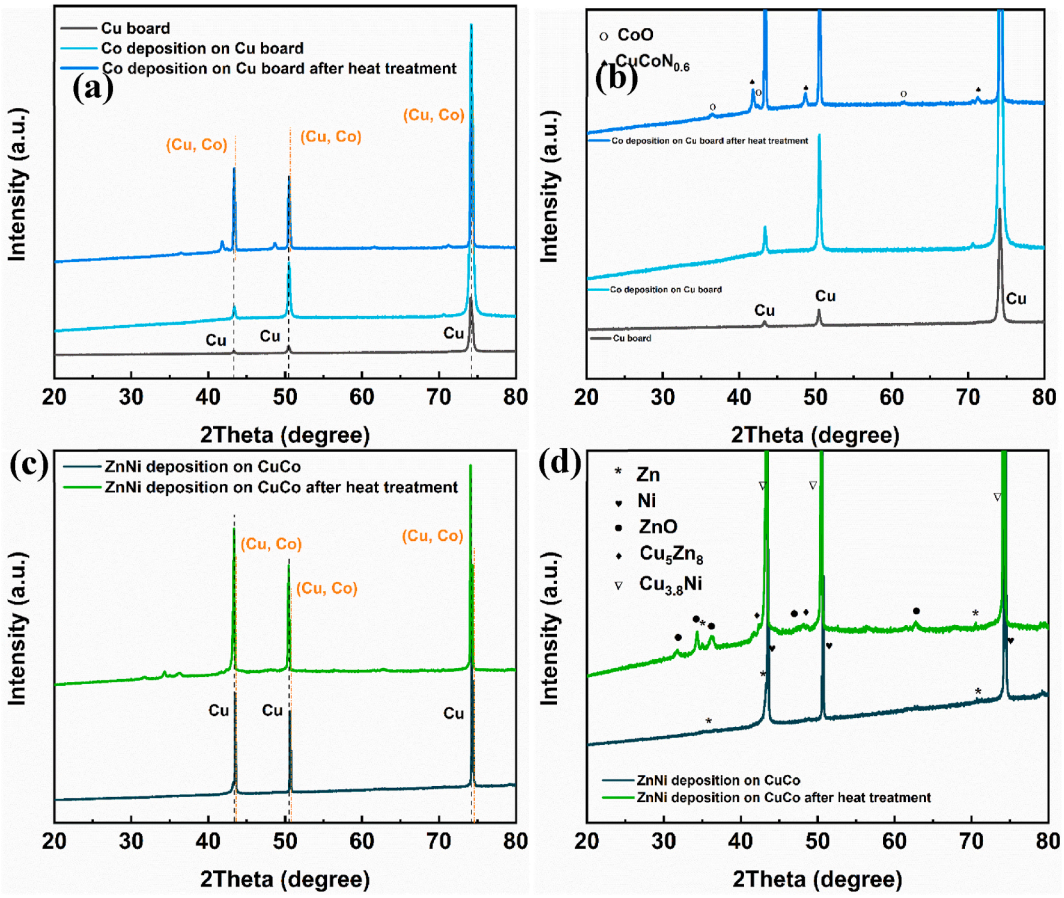

Fig. 3. XRD patterns of a 1 h deposited Co on Cu before (a) and after (b) heat treatment, and deposited Zn–Ni on Cu–Co alloys before (a) and after (b) heat treatment.

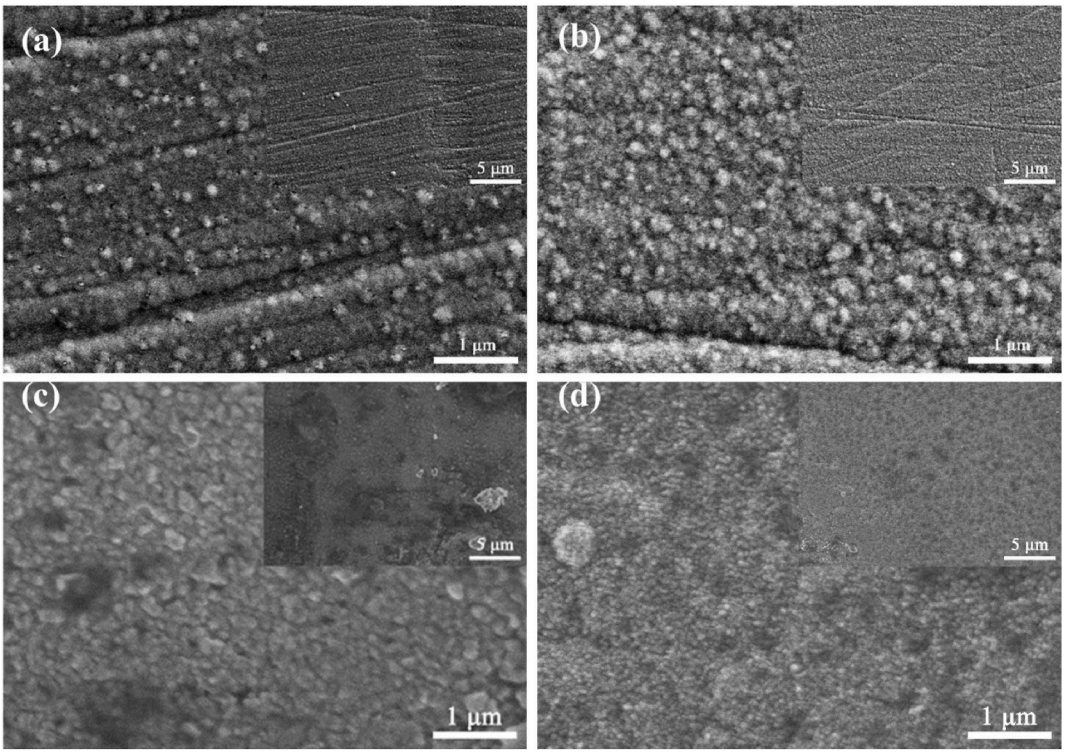

Fig. 4. SEM images of a 1 h deposited Co on Cu before (a) and after (b) heat treatment, (c) 2 h deposited Zn–Ni on Cu–Co alloys before (c) and after (d) heat treatment.

Table 2
Elemental composition of the different alloys before and after heat treatment.

	Parameters	Heat treatment	Zn (at%)	Ni (at%)	Co (at%)	Cu (at%)	O (at%)
Co on Cu foil	−1.05 V, 60 °C, 60 min	No	–	–	61.7	25.8	12.5
		Yes	–	–	50.6	35.5	13.8
Zn–Ni on Co–Cu	−1.3 V, 40 °C, 120 min	No	68.1	10.0	8.1	3.6	10.3
		Yes	55.0	9.9	4.0	8.7	22.4

diffusion of inner Cu to the surface, resulting in the formation of an alloy with a final composition of $Zn_{70.9}Ni_{12.7}Cu_{11.2}Co_{5.2}$.

As previously discussed, although the distribution of elements following the heat treatment seems comparatively more uniform than the one observed prior to the heat treatment, it is challenging to ascertain the distribution of elements within the deposited film based solely on the analysis of surface elements. A more detailed distribution can be obtained through line scanning with EDS, as illustrated in Fig. S3. Due to the ductility of copper, there is a possibility that some copper may be incorporated into the deposit during the preparation of the SEM sample. However, the individual elements can still be identified. Following electrodeposition, it is clear that the Co is distinctly separated from the substrate. At a depth of 1.4 μm below the surface (corresponding to the initial measurement), the Co signal is no longer discernible and a substantial quantity of copper is detected corresponding to the copper substrate on which the deposit was performed. After the heat treatment, the lateral and top surfaces were measured concurrently due to the fixed angle of the sample for the EDS analysis. The higher Cu content was observed in the fractured portion of the deposit and at the boundary between the deposit and the Cu substrate. This suggests that during the heat treatment process, diffusion occurred between the Co and Cu phases. The higher Cu content in comparison to Co can be attributed to the penetration depth of the electron beam, which results in the detection of the Cu from the substrate. Additionally, the introduction of Cu particles from the substrate into the deposit during the preparation of the sample for SEM observation represents another source of contamination. The electrodeposition of a Zn–Ni alloy on a Co–Cu alloy resulted in a higher concentration of Zn at a depth of 15 μm, while Cu was undetectable at this location. After the heat treatment, the topography, as illustrated in Fig. S3d, demonstrates the presence of two discrete thin films on the surface of the sample. The analysis of the element distribution at the double film level shows that the Zn distribution is nearly uniform, spanning a range of 1.0–1.7 μm from the surface. Concurrently, the Ni content relatively low, yet its distribution position remains consistent with that of Zn, exhibiting a certain uniformity. In contrast, the distribution of Cu is progressive, with the highest concentration observed in regions situated farther from the surface of the alloy. The Co is predominantly concentrated in the second film (i.e., the Co–Cu substrate) and the Cu substrate. A residual quantity of Co signal is observed when the surface is scanned. Indeed, the analysis of the element distribution and morphology of the final Zn–Ni–Co–Cu alloy, obtained following heat treatment, indicates that Ni and Zn are uniformly distributed in the two deposit layers. Conversely, the Co content is lower in the upper layer of deposits (Zn–Ni deposits), with the majority of this element is concentrated in the second layer (Co–Cu). As Cu diffuses from the Cu substrate to the upper layer, its distribution gradually decreases. It can therefore be assumed that this alloy, which exhibits a distribution of elements, could also present nanopores distributed unevenly after dealloying, thus offering various opportunities in the field of dealloying research.

The $Zn_{70.9}Ni_{12.7}Cu_{11.2}Co_{5.2}$ alloy was chemically dealloyed in a series of solutions, including EAN +0.01 M CH_3COOH, 1 M KOH, 0.01 M HNO_3, 0.1 M H_3PO_4, and 1 M H_3PO_4 aqueous solutions. Electrochemical dealloying was performed in a 1 M KOH aqueous solution at 1.09 V/RHE for varying periods of time, in agreement with the CV curves presented in Fig. 2d, which correspond to Cu oxidation. The dealloying procedures were with great care under an argon flow to minimize the formation of oxides.

Fig. 5a and b shows the SEM micrographs of the chemical dealloying process in EAN +0.01 M CH_3COOH. After a 3-min treatment period, the alloy surface displays an irregular morphology. After a 5-min treatment, a characteristic pore structure emerges and becomes evenly distributed across the alloy surface. The full range of pore widths observed spanned approximately from 100 to 400 nm. The outcomes of a half-hour treatment for alloys that underwent chemical dealloying in a 1 M KOH solution are illustrated in Fig. 5c and d. These figures demonstrate the emergence of grooves on the surface and the formation of dense and uniform pores with a diameter of 100 nm. Conversely, a 1-h dealloying period results in a flat surface with numerous cracks, indicating that an excessively prolonged dealloying time leads to the destruction of the surface structure. The resulting morphology from electrochemical dealloying in KOH is presented in Fig. 5e and f. It is noteworthy that dense, homogeneous nanopores with an average width of approximately 100 nm have been demonstrated to form on the surface after just 10 min of polarization. A comparison of the samples treated for 10- and 30-min reveals that a longer electrochemical dealloying process results in an increase in pore size, which eventually connects to form cracks and grooves. These results can be compared to those of a chemical dealloying process conducted in HNO_3, which yielded a comparable porous structure. Fig. S4 presents the cross-section of the HNO_3-treated sample, which demonstrates that the porous structure caused by dealloying is not limited to the sample surface, but rather penetrates through the entire alloy film. The morphology of the alloy surface after chemical dealloying in H_3PO_4 shows a more continuous pore structure, as illustrated in Fig. 5h and i. This was particularly evident in the 30-min dealloying procedure carried out in 0.1 M H_3PO_4, where the results showed a more homogeneous distribution and size of nanopores than in HNO_3. These findings indicates that the dealloying process can generate nanoporous structures with controllable pore size and distribution.

The elemental composition of the nanoporous alloy resulting from dealloying is presented in Fig. S5 and summarized in Table S2. These findings show that the quantity of zinc present in the alloy underwent a significant decrease during the dealloying process, regardless the dealloying technique employed, whether chemical or electrochemical. In particular, after a 30 min dealloying process in HNO_3, no Zn was detected at the surface. A decreased of the Zn content to 10.5 at% after dealloying at a potential of 1.09 V for 10 min in 1.0 M KOH solution. This also indicates that, at this potential, Zn in the alloy can be successfully removed. Notwithstanding the fact that, in the case of the nanoporous alloys prepared in HNO_3, Zn constitutes the principal element on the surface, they also show a low oxygen content on the surface. In contrast, the majority of samples exhibited a notable increase in nickel content. Concerning the copper content, the initial value was 8.7 at%, and in the majority of cases, an increase was observed following dealloying. A dealloying potential of 1.09 V/Ag/Ag^+ results in the stripping of Cu. However, the distribution of Cu exhibits a gradient from the surface of the top layer (Zn–Ni deposits) inside the alloy (according to line scan EDS analysis). Consequently, the electrochemical dealloying in KOH solution resulted in the exposure of a greater quantity of Cu, reaching 15.8 and 22.2 at%, respectively.

The distribution of elements in alloys can be more accurately determined through the use of EDS mapping and line scan, as shown in Fig. 6, which was obtained for the alloy $Cu_{30.0}Ni_{29.7}Co_{25.2}Zn_{15.1}$ that has undergone electrochemical dealloying in 1 M KOH at 1.09 V/RHE for 30

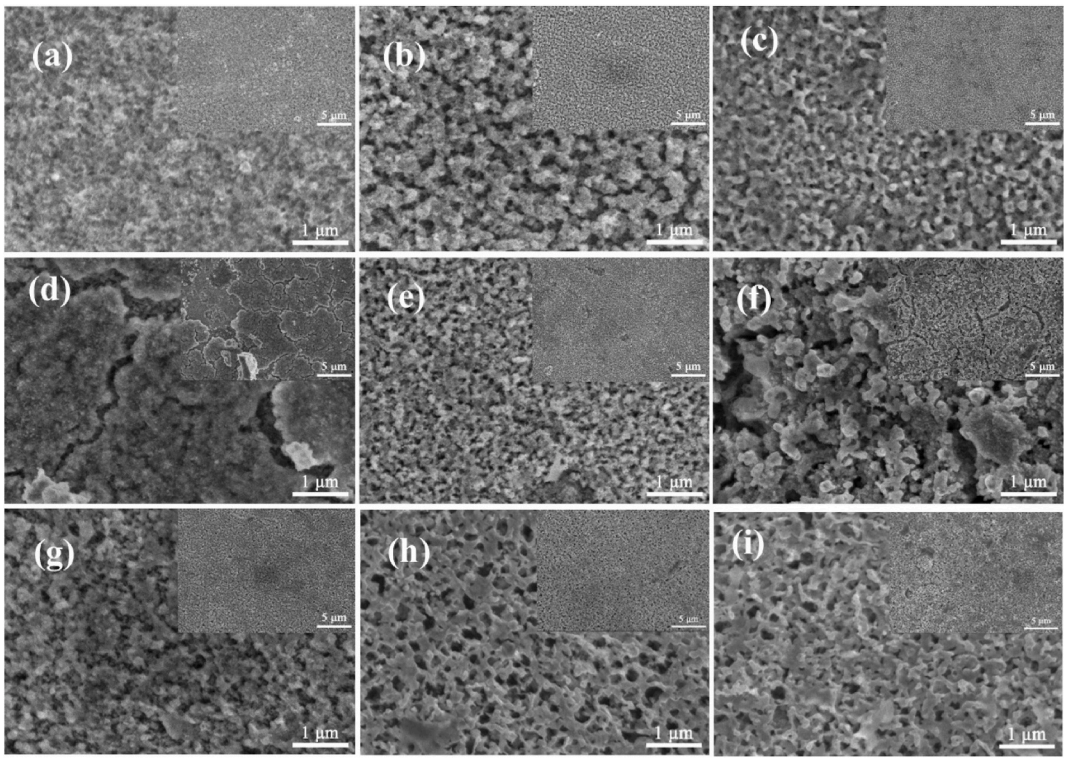

Fig. 5. *SEM micrographs of Cu–Zn–Ni–Co alloys treated in EAN + 0.01 M CH_3COOH for* 3 min *(a) and* 5 min *(b); in 1 M KOH for* 30 min *(c) and* 60 min *(d) and electrochemical dealloying in 1 M KOH at 1.09 V/RHE for* 10 min *(e) and* 30 min *(f); in 0.01 M HNO_3 for* 30 min *(g); in 0.1 M H_3PO_4 for* 30 min *(h) and in 1 M H_3PO_4 for* 10 min*(i)*.

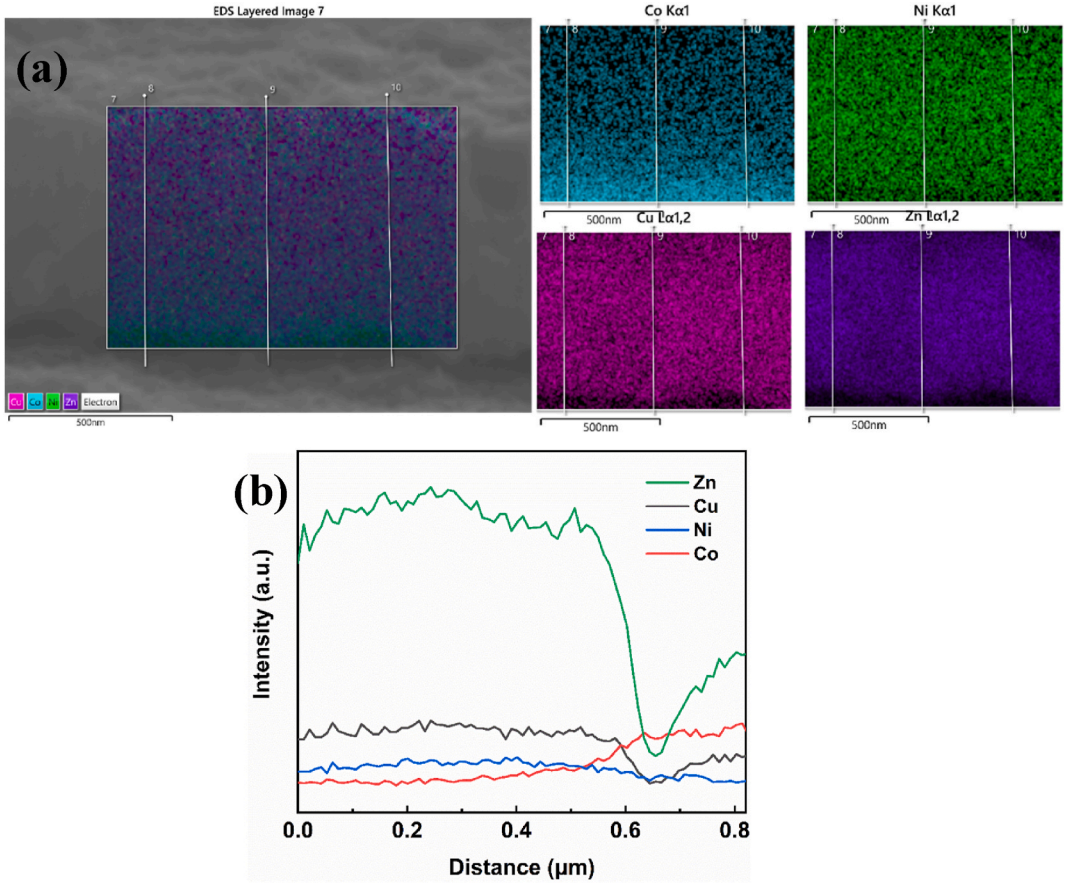

Fig. 6. *EDS analysis of the $Cu_{30.0}Ni_{29.7}Co_{25.2}$ $Zn_{15.1}$ film cross-section: (a) mapping scan, and (b) line scan.*

min. As illustrated in Fig. 6 and Table S3, the constituent elements of the alloy show a gradient in their distribution. The global mapping data and the point data from the line scan both indicate a relatively uniform distribution of Cu and a continuous decrease in Ni from the surface to the deeper layers. However, the distribution of Zn exhibits an intriguing pattern, displaying a slight increase from the surface and then a subsequent decrease towards the interior. Specifically, the Zn content increases from 65.1 at% at the surface to 71.5 at% at some depth, where it then decreases to 48.4 at% in the deeper layers. This shows that Zn was removed from the surface during the dealloying process and diffused from the primary layer to the interior after the heat treatment.

XPS analysis was used to study the surface state of dealloyed nanoporous alloys made in different solutions. This discussion focuses on the Ni, which is important for its electrocatalytic properties. Fig. 7a shows that the dealloyed alloy in 1 M KOH for 30 min, $Zn_{70.3}Ni_{15.7}Co_{8.6}Cu_{5.4}$, has main peaks for Ni(II) (NiO 855.7 eV, $Ni(OH)_2$ 856.0 eV). NiO and $Ni(OH)_2$ originate from the oxidation that occurs during the transfer of the samples and the dealloying process. Furthermore, the quantity of $Ni(OH)_2$ is significantly greater than that of NiO, as evidenced by a comparison of the peak areas. The original alloy ($Zn_{70.9}Ni_{12.7}Cu_{11.2}Co_{5.2}$, Fig. S6) is similar to the present sample. The $Zn_{38.5}Co_{23.8}Ni_{23.1}Cu_{14.6}$ sample, prepared in 0.1 M H_3PO_4 for 30 min, shows peaks corresponding to Ni(0) (852.8 eV), Ni(II) (NiO 854.1 eV, $Ni(OH)_2$ 855.3 eV, $Ni_3(PO_4)_2$, 853.7 eV), respectively [27,35]. The ratio of NiO to $Ni(OH)_2$ is unchanged. However, it it has a strong peak for Ni(0), which is more noticeable than for $Zn_{70.3}Ni_{15.7}Co_{8.6}Cu_{5.4}$. Obviously, there are more Ni (0) distributed on the alloy surface after the dealloying in H_3PO_4 solution. During dealloying, Ni is rearranged and redistributed, dissolving and becoming dispersed on the surface. Furthermore, it is acknowledged that this rearrangement phenomenon extends to other alloy constituents, thereby contributing to the mechanism by which dealloying facilitates the formation of nanoporous structures [24,36]. Additionally, phosphoric acid anions remain in the deposit due to a combination of PO_4^{3-} ions with the alloys at the electrode surface. The chemical state of Co on the surface of $Zn_{38.5}Co_{23.8}Ni_{23.1}Cu_{14.6}$ can be observed in Fig. S6c, which shows that the surface consists mainly of Co_3O_4 (780.0eV, 781.3eV, 782.6eV, 785.6eV and 789.9eV). This suggests that during the dealloying process, the surface Co preferentially tends to form oxides.

3.3. Electrocatalytic hydrogen evolution reaction of water by nanoporous alloys

The effective electrochemical surface area (ECSA) of nanoporous alloys was determined by evaluating the interfacial capacitance (C^{σ}) at various scan rates, as illustrated in Fig. 8a. The post-dealloying C^{σ} value is much higher than that of the original alloy, $Zn_{70.9}Ni_{12.7}Cu_{11.2}Co_{5.2}$ (0.23 mF cm^{-2}), with a maximum value reaching 0.84 mF cm^{-2}, corresponding to $Ni_{36.7}Zn_{36.0}Co_{18.7}Cu_{8.6}$. Although the presence of oxides could influence the results, the examination of Table S2 shows that the oxidation level is uniform across samples, except for the nanoporous alloys made in H_3PO_4, which had the least oxygen. This suggests that the oxide effect is minimal and that the increase in ECSA after dealloying is due to the formation of a nanoporous structure.

Fig. 8b shows the electrocatalytic performance of the nanoporous alloys, which have distinctive characteristics; the values of the electrocatalytic properties are shown in Table 3. It is noteworthy that compositions such as $Zn_{70.3}Ni_{15.7}Co_{8.6}Cu_{5.4}$, $Ni_{36.7}Zn_{36.0}Co_{18.7}Cu_{8.6}$, $Ni_{66.9}Cu_{18.5}Zn_{12.3}Co_{2.3}$, and $Cu_{30.0}Ni_{29.7}Co_{25.2}Zn_{15.1}$, prepared in KOH solution, exhibited remarkably low HER potential values of −0.084 V/RHE, −0.074 V/RHE, −0.071 V/RHE, and −0.067 V/RHE, respectively, which is closed to the HER potential of the cycled 10 wt% Pt–C (−0.078 V/RHE) [37]. These results indicate that these nanoporous alloys prepared in KOH solution have a lower HER potential and higher HER performance compared to the original alloy $Zn_{70.9}Ni_{12.7}Cu_{11.2}Co_{5.2}$ (−0.102 V/RHE). The nanoporous alloys prepared in KOH solutions are also better in HER potential than some Ni-based alloys studied in other works under similar conditions, such as the deposited Ni–Zn, Al–Ni–P form and the nanoporous alloy np-NiFeMoP with HER potentials of −0.068 V/RHE, −0.111 V/RHE and −0.223 V/RHE, respectively [38–40]. The nanoporous materials, which are obtained by chemical dealloying in acidic solution, exhibit higher potentials for the HER compared to the pristine alloy. While a sample prepared by dealloying in EAN +0.01 M CH_3COOH, corresponding to the composition $Co_{37.4}Zn_{29.3}Cu_{24.1}Ni_{9.2}$, did not show an optimal HER overpotential value, it exhibited the lowest Tafel slope (55.5 mV·dec^{-1}). It is interesting to note that nanoporous alloys, specifically $Zn_{38.5}Co_{23.8}Ni_{23.1}Cu_{14.6}$ and $Zn_{38.9}Cu_{23.3}Ni_{19.6}Co_{18.2}$, which underwent dealloying in H_3PO_4, exhibited significantly higher overpotential values but significantly reduced Tafel slopes compared to their original non-porous alloy, $Zn_{70.9}Ni_{12.7}Cu_{11.2}Co_{5.2}$.

XPS analysis shows that the surface rearrangement of the alloying elements post-dealloying disrupts the original alloy structure and reduces the electrocatalytic performances [27,41]. In addition, the presence of phosphate species on the surface of the material hinders solution contact, which in turn leads to an increase in the HER potential value and worse HER performances compared to other alloys. SEM observations in conjunction with C^{σ} measurements indicate that these dealloyed alloys have a greater number of contiguous pores and a higher electrochemical surface area, which can provide a more active point and a higher reaction rate during the water splitting process, resulting in to a lower Tafel slope. Furthermore, the alloy with a composition of $Ni_{66.9}Cu_{18.5}Zn_{12.3}Co_{2.3}$ exhibited a lower Tafel slope of 70.8 mV·dec^{-1}.

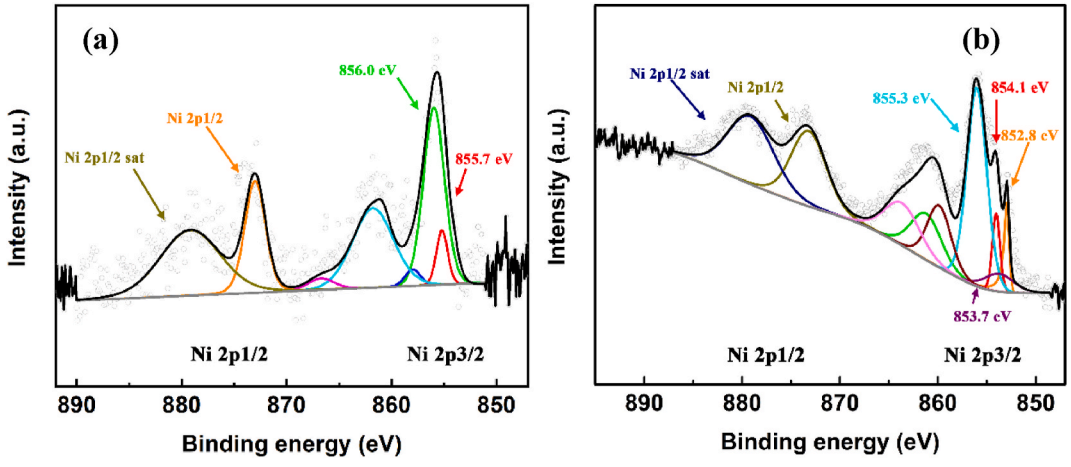

Fig. 7. *XPS spectra of different nanoporous alloys. a) Ni 2p of $Zn_{70.3}Ni_{15.7}Co_{8.6}Cu_{5.4}$, b) Ni 2p of $Zn_{38.5}Co_{23.8}Ni_{23.1}Cu_{14.6}$.*

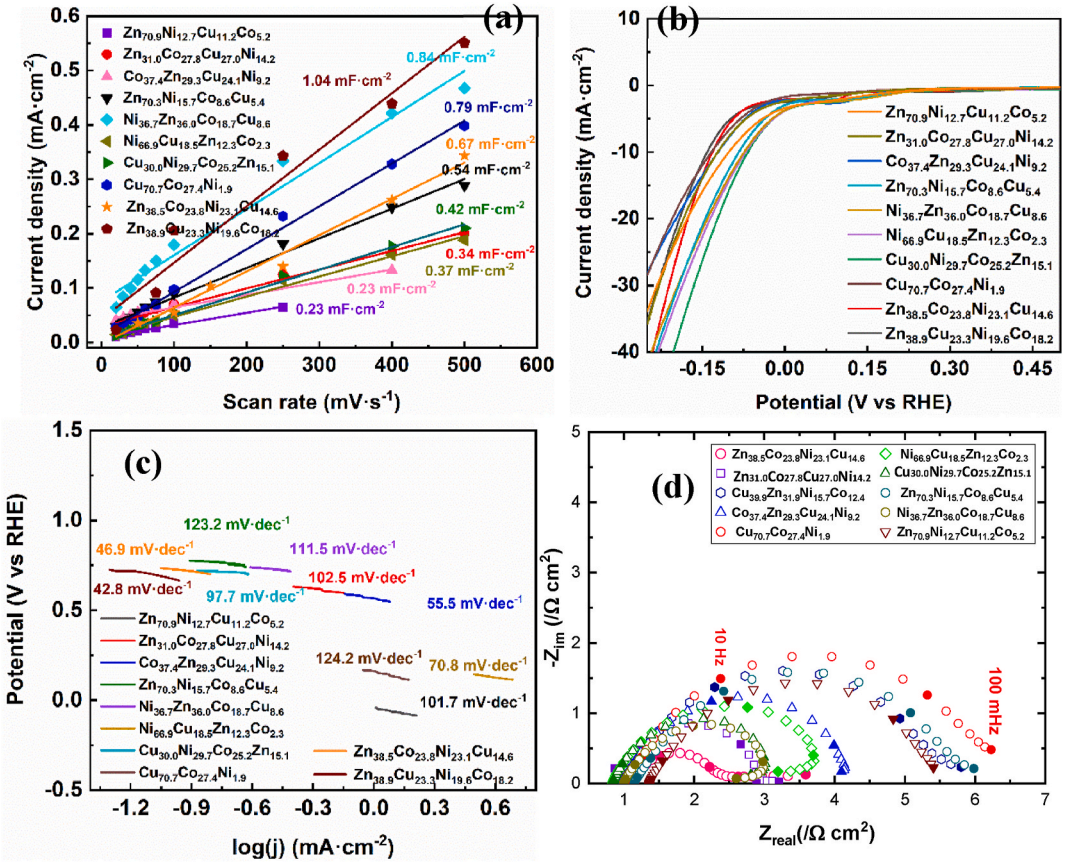

Fig. 8. *Electrocatalytic properties of the materials towards the HER for nanoporous Cu–Zn–Ni–Co alloys: C^{σ} (a), LSV curves (b), Tafel slopes (c) and EIS curves (d).*

Table 3
Electrochemical properties of nanoporous Cu–Zn–Ni–Co alloys towards the HER.

	C^{σ} (mF·cm^{-2})	HER potential (V/RHE)	Tafel slope (mV·dec^{-1})	R_{ct} (Ω cm^2)
$Zn_{70.9}Ni_{12.7}Cu_{11.2}Co_{5.2}$	0.23	−0.102	101.7	4.0
$Zn_{31.0}Co_{27.8}Cu_{27.0}Ni_{14.2}$	0.34	−0.122	102.5	4.5
$Co_{37.4}Zn_{29.3}Cu_{24.1}Ni_{9.2}$	0.23	−0.121	55.5	3.1
$Zn_{70.3}Ni_{15.7}Co_{8.6}Cu_{5.4}$	0.54	−0.084	123.2	4.6
$Ni_{36.7}Zn_{36.0}Co_{18.7}Cu_{8.6}$	0.84	−0.074	111.5	2.0
$Ni_{66.9}Cu_{18.5}Zn_{12.3}Co_{2.3}$	0.37	−0.071	70.8	2.8
$Cu_{30.0}Ni_{29.7}Co_{25.2}Zn_{15.1}$	0.42	−0.067	97.7	2.1
$Cu_{70.7}Co_{27.4}Ni_{1.9}$	0.79	−0.133	124.2	5.1
$Zn_{38.5}Co_{23.8}Ni_{23.1}Cu_{14.6}$	0.67	−0.133	46.9	1.2
$Zn_{38.9}Cu_{23.3}Ni_{19.6}Co_{18.2}$	1.04	−0.124	42.8	2.0

The distribution of the primary elements on the top surface of this nanoporous alloy, mainly Cu and Ni, contributes to its improved electrocatalytic performance compared to alloys with higher Zn content.

The impedance of the alloys allows to easy evaluation of the electrolyte resistance (R_s) and charge transfer resistance (R_{ct}) of the HER. In this case, the equivalent circuit can be described as a one-time constant model [42]. As shown in Fig. 8d, the electrochemical dealloying procedure effectively reduces the charge transfer resistance, as exemplify by the impedance spectra. Indeed, compositions such as $Ni_{36.7}Zn_{36.0}Co_{18.7}Cu_{8.6}$ and $Ni_{66.9}Cu_{18.5}Zn_{12.3}Co_{2.3}$ exhibit lower charge transfer resistances values of 2.0 and 2.8 Ω cm^2, respectively, compared to the original alloy, $Zn_{67.3}Ni1_{8.3}Cu_{7.8}Co_{6.6}$, which exhibits a charge transfer resistance of 4.0 Ω cm^2. It is important to note at this point that the impedance plots are plotted using the real surface area (i.e., the ECSA values). These results indicate that the electrochemical dealloying has a beneficial effect on the electron transfer kinetics at the surface of the nanoporous alloy. The exchange current densities j_0 for different samples are presented in Fig. S7. These values were calculated using established methods from previous literature, with Pt/C serving as the benchmark j_0 (0.75 mA cm^{-2}). Most samples did not exhibit significant differences in j_0, however, the $Co_{37.4}Zn_{29.3}Cu_{24.1}Ni_{9.2}$ alloy demonstrated a notably higher j_0 value of 0.546 mA cm^{-2}, accompanied by a superior Tafel slope. This indicates that the $Co_{37.4}Zn_{29.3}Cu_{24.1}Ni_{9.2}$ catalyst possesses more efficient catalytic performance for HER [43]. The post-HER surface state of the catalyst is also of great interest. As shown in Fig. S8a, the oxygen content on the surface increased significantly from 13.0 at% to 34.9 at%, while the cobalt content became more prominent, rising from 7.5 at% to 28.8 at%. This observation is consistent with the XPS results, which indicate that Co tends to form strong bonds with oxygen. Additionally, SEM images in Fig. S8b reveal that the surface is covered with tablet-like particles, which can be referred to the oxidation on Co and Ni on the surface.

In the context of catalysts, the issue of reusability is of paramount importance. After ten cycles, the nanoporous materials, $Zn_{38.5}Co_{23.8}Ni_{23.1}Cu_{14.6}$, dealloyed in H_3PO_4 showed a significant increase in overpotential, with an increase of 130 %, while the nanoporous alloy, $Zn_{70.3}Ni_{15.7}Co_{8.6}Cu_{5.4}$ showed an increase in HER potential of 48 %, as shown in Fig. S9a. In addition, it was observed that there was significant surface alloy delamination at the end of the reaction process. Conversely, the $Zn_{70.3}Ni_{15.7}Co_{8.6}Cu_{5.4}$ alloy obtained after a 30 min treatment in KOH show only a 10 % overpotential increase during the 50 h of galvanostatic testing (performed at the threshold current of −10 mA cm^{-2}), as illustrated in Fig. S9b. This indicates a better stability compared to the H_3PO_4-treated alloy. These results suggest that alloys with Ni, Cu, and Co as the main elements and exhibiting a uniform distribution of nanopores have the potential to serve as highly effective electrocatalysts. Consequently, future efforts could be directed toward

precisely modulating of the structure and composition of alloy film on the electrode surface by carefully controlling the dealloying and heat treatment parameters of multi-component alloys.

4. Conclusions

This study presents the preparation of nanoporous Cu–Zn–Ni–Co alloys with varying compositions by electrodeposition in EAN and ethaline, followed by heat treatment and dealloying in acid and alkaline solutions. Additionally, the properties of these alloys for the HER were investigated. Nanoporous alloys show interesting characteristics in terms of morphology, element distribution, and properties for the HER. The impact of varying dealloying conditions, especially the choice of solution (CH_3COOH in EAN, KOH, HNO_3 and H_3PO_4), on the morphology and element distribution of the nanoporous alloys was investigated. It has been shown that Zn is the most easily removed element from the alloy, leaving vacancies that facilitate pore formation. Compared to the original non-porous alloy, the HER performance is significantly improved, with a HER potential as low as −0.067 V/RHE. The improvement in performance depends on a combination of the specific surface area and element distribution of the alloys. This study demonstrates that the electrochemical preparation of quaternary alloys consisting of Cu, Ni, Zn, and Co, can be achieved through electrodeposition and heat treatment. The different deposits are combined through diffusion during the annealing process. Furthermore, the nanoporous alloy structure can be prepared and controlled through chemical dealloying and electrochemical dealloying, which opens new avenues for the prospective application of nanoporous alloy electrodes in the electrocatalysis.

CRediT authorship contribution statement

Yuelin Xie: Writing – review & editing, Writing – original draft, Validation, Methodology, Investigation, Formal analysis, Data curation, Conceptualization. **Antoine Miche:** Writing – review & editing, Investigation, Formal analysis. **Vincent Vivier:** Writing – review & editing, Writing – original draft, Validation, Supervision, Project administration, Methodology, Formal analysis, Data curation, Conceptualization. **Mireille Turmine:** Writing – review & editing, Writing – original draft, Validation, Supervision, Project administration, Methodology, Formal analysis, Data curation, Conceptualization.

Declaration of competing interest

The authors declare the following financial interests/personal relationships which may be considered as potential competing interests.

Yuelin Xie reports financial support was provided by China Scholarship Council. If there are other authors, they declare that they have no known competing financial interests or personal relationships that could have appeared to influence the work reported in this paper.

Acknowledgements

Yuelin XIE was supported by the China Scholarship Council for 3-year PhD project at the Sorbonne Université.

Appendix A. Supplementary data

Supplementary data to this article can be found online at https://doi.org/10.1016/j.ijhydene.2025.04.067.

References

[1] Feng H, Yu J, Tang L, Wang J, Dong H, Ni T, Tang J, Tang W, Zhu X, Liang C. Improved hydrogen evolution activity of layered double hydroxide by optimizing the electronic structure. Appl Catal B Environ 2021;297:120478.
[2] Ahmad S, Ullah A, Samreen A, Qasim M, Nawaz K, Ahmad W, Alnaser A, Kannan AM, Egilmez M. Hydrogen production, storage, transportation and utilization for energy sector: a current status review. J Energy Storage 2024;101:113733.
[3] Bachvarov V, Lefterova E, Rashkov R. Electrodeposited NiFeCo and NiFeCoP alloy cathodes for hydrogen evolution reaction in alkaline medium. Int J Hydrogen Energy 2016;41(30):12762–71.
[4] Laszczyńska A, Szczygieł I. Electrocatalytic activity for the hydrogen evolution of the electrodeposited Co–Ni–Mo, Co–Ni and Co–Mo alloy coatings. Int J Hydrogen Energy 2020;45(1):508–20.
[5] Lian J, Wu Y, Zhang H, Gu S, Zeng Z, Ye X. One-step synthesis of amorphous Ni–Fe–P alloy as bifunctional electrocatalyst for overall water splitting in alkaline medium. Int J Hydrogen Energy 2018;43(29):12929–38.
[6] Gong M, Wang D-Y, Chen C-C, Hwang B-J, Dai H. A mini review on nickel-based electrocatalysts for alkaline hydrogen evolution reaction. Nano Res 2016;9(1):28–46.
[7] Karimzadeh A, Aliofkhazraei M, Walsh FC. A review of electrodeposited Ni-Co alloy and composite coatings: microstructure, properties and applications. Surf Coat Technol 2019;372:463–98.
[8] Ahmad S, Egilmez M, Abuzaid W, Mustafa F, Kannan AM, Alnaser AS. Efficient medium entropy alloy thin films as bifunctional electrodes for electrocatalytic water splitting. Int J Hydrogen Energy 2024;52:1428–39.
[9] Ahmad S, Egilmez M, Shanmugam R, Abuzaid W, Sharma S, Gangavarapu RR, Mustafa F, El-Khatib S, Alawadhi H, Kannan AM. Electrochemical hydrogen evolution reaction evaluation of CoNi(Cr/V) medium-entropy alloys in an acidic environment. ACS Appl Energy Mater 2023;6(20):10652–64.
[10] Cui X, Chen M, Xiong R, Sun J, Liu X, Geng B. Ultrastable and efficient H2 production via membrane-free hybrid water electrolysis over a bifunctional catalyst of hierarchical Mo–Ni alloy nanoparticles. J Mater Chem A 2019;7(27):16501–7.
[11] Chen L, Yang S, Qian K, Wei W, Sun C, Xie J. In situ growth of N-doped carbon coated CoNi alloy with graphene decoration for enhanced HER performance. J Energy Chem 2019;29:129–35.
[12] Im SW, Ahn H, Seo DH, Park S, Choi S, Ryu W, Kim K, Park ES, Nam KT. A scalable Al–Ni alloy powder catalyst prepared by metallurgical microstructure control. J Mater Chem A 2020;8(22):11133–40.
[13] Skibińska K, Kutyła D, Kula A, Gajewska M, Marzec MM, Żabiński P. Hydrogen evolution reaction (HER) activity of conical Co–Fe alloy structures and their application as a sensitive and rapid sensor for H2O2 detection. Arch Civ Mech Eng 2022;22(2):76.
[14] Sequeira CAC, Santos DMF, Brito PSD. Electrocatalytic activity of simple and modified Fe–P electrodeposits for hydrogen evolution from alkaline media. Energy 2011;36(2):847–53.
[15] Patil RB, Mantri A, House SD, Yang JC, McKone JR. Enhancing the performance of Ni-Mo alkaline hydrogen evolution electrocatalysts with carbon supports. ACS Appl Energy Mater 2019;2(4):2524–33.
[16] González-Buch C, Herraiz-Cardona I, Ortega E, García-Antón J, Pérez-Herranz V. Synthesis and characterization of macroporous Ni, Co and Ni–Co electrocatalytic deposits for hydrogen evolution reaction in alkaline media. Int J Hydrogen Energy 2013;38(25):10157–69.
[17] Zhang X, Li Y, Guo Y, Hu A, Li M, Hang T, Ling H. 3D hierarchical nanostructured Ni–Co alloy electrodes on porous nickel for hydrogen evolution reaction. Int J Hydrogen Energy 2019;44(57):29946–55.
[18] Lotfi N, Shahrabi T, Yaghoubinezhad Y, Darband GB. Surface modification of Ni foam by the dendrite Ni-Cu electrode for hydrogen evolution reaction in an alkaline solution. J Electroanal Chem 2019;848:113350.
[19] Herraiz-Cardona I, Ortega E, Pérez-Herranz V. Impedance study of hydrogen evolution on Ni/Zn and Ni–Co/Zn stainless steel based electrodeposits. Electrochim Acta 2011;56(3):1308–15.
[20] Ahmad S, Boltaev G, Egilmez M, Abuzaid W, Alawadhi H, Kannan AM, Alnaser AS. Impact of femtosecond laser surface structuring on NiCoCr and NiCoV medium entropy alloy systems for an overall electrochemical water splitting. Int J Hydrogen Energy 2024;59:1094–105.
[21] Shetty S, Hegde AC. In *A Study on composition dependent electrocatalytic Behaviour of electrodeposited Ni-Mo alloy*. Nano hybrids and composites. Trans Tech Publ; 2017. p. 113–20.
[22] Dan Z, Qin F, Sugawara Y, Muto I, Hara N. Fabrication of nanoporous copper by dealloying amorphous binary Ti–Cu alloys in hydrofluoric acid solutions. Intermetallics 2012;29:14–20.
[23] Zhang C, Sun J, Xu J, Wang X, Ji H, Zhao C, Zhang Z. Formation and microstructure of nanoporous silver by dealloying rapidly solidified Zn–Ag alloys. Electrochim Acta 2012;63:302–11.
[24] Li R, Liu XJ, Wang H, Zhou DQ, Wu Y, Lu ZP. Formation mechanism and characterization of nanoporous silver with tunable porosity and promising capacitive performance by chemical dealloying of glassy precursor. Acta Mater 2016;105:367–77.
[25] Wu L, Hofmann JP. Comparing the intrinsic HER activity of transition metal dichalcogenides: pitfalls and suggestions. ACS Energy Lett 2021;6(7):2619–25.
[26] Huang JH, Kargl-Simard C, Oliazadeh M, Alfantazi AM. pH-Controlled precipitation of cobalt and molybdenum from industrial waste effluents of a cobalt electrodeposition process. Hydrometallurgy 2004;75(1):77–90.
[27] Xie Y, Miche A, Vivier V, Turmine M. Electrodeposition of Ni-Co alloys from neat protic ionic liquid: application to the hydrogen evolution reaction. Appl Surf Sci 2023:157693.

[28] Koh S, Strasser P. Electrocatalysis on bimetallic surfaces: modifying catalytic reactivity for oxygen reduction by voltammetric surface dealloying. J Am Chem Soc 2007;129(42):12624–5.
[29] Medway SL, Lucas CA, Kowal A, Nichols RJ, Johnson D. In situ studies of the oxidation of nickel electrodes in alkaline solution. J Electroanal Chem 2006;587 (1):172–81.
[30] Bing L, Huatang Y, Yunshi Z, Zuoxiang Z, Deying S. Cyclic voltammetric studies of stabilized α-nickel hydroxide electrode. J Power Sources 1999;79(2):277–80.
[31] Wang JM, Zhang L, Zhang C, Zhang JQ. Effects of bismuth ion and tetrabutylammonium bromide on the dendritic growth of zinc in alkaline zincate solutions. J Power Sources 2001;102(1):139–43.
[32] Ko Y, Park S-M. Zinc oxidation in dilute alkaline solutions studied by real-time electrochemical impedance spectroscopy. J Phys Chem C 2012;116(13):7260–8.
[33] Zhang QB, Abbott AP, Yang C. Electrochemical fabrication of nanoporous copper films in choline chloride–urea deep eutectic solvent. Phys Chem Chem Phys 2015; 17(22):14702–9.
[34] Cai J, Xu J, Wang J, Zhang L, Zhou H, Zhong Y, Chen D, Fan H, Shao H, Zhang J. Fabrication of three-dimensional nanoporous nickel films with tunable nanoporosity and their excellent electrocatalytic activities for hydrogen evolution reaction. Int J Hydrogen Energy 2013;38(2):934–41.
[35] Mirghni AA, Madito MJ, Oyedotun KO, Masikhwa TM, Ndiaye NM, Ray SJ, Manyala N. A high energy density asymmetric supercapacitor utilizing a nickel phosphate/graphene foam composite as the cathode and carbonized iron cations adsorbed onto polyaniline as the anode. RSC Adv 2018;8(21):11608–21.
[36] Luo X, Li R, Huang L, Zhang T. Nucleation and growth of nanoporous copper ligaments during electrochemical dealloying of Mg-based metallic glasses. Corros Sci 2013;67:100–8.
[37] Hu YC, Wang YZ, Su R, Cao CR, Li F, Sun CW, Yang Y, Guan PF, Ding DW, Wang ZL, Wang WH. A highly efficient and self-stabilizing metallic-glass catalyst for electrochemical hydrogen generation. Adv Mater 2016;28(46):10293–7.
[38] Zhang H, Feng Z, Wang L, Li D, Xing P. Bifunctional nanoporous Ni-Zn electrocatalysts with super-aerophobic surface for high-performance hydrazine-assisted hydrogen production. Nanotechnology 2020;31(36):365701.
[39] Qian H, Li K, Mu X, Zou J, Xie S, Xiong X, Zeng X. Nanoporous NiFeMoP alloy as a bifunctional catalyst for overall water splitting. Int J Hydrogen Energy 2020;45 (33):16447–57.
[40] Lado JL, Wang X, Paz E, Carbó-Argibay E, Guldris N, Rodríguez-Abreu C, Liu L, Kovnir K, Kolen'ko YV. Design and synthesis of highly active Al–Ni–P foam electrode for hydrogen evolution reaction. ACS Catal 2015;5(11):6503–8.
[41] Chen M, Liu D, Zi B, Chen Y, Liu D, Du X, Li F, Zhou P, Ke Y, Li J. Remarkable synergistic effect in cobalt-iron nitride/alloy nanosheets for robust electrochemical water splitting. J Energy Chem 2022;65:405–14.
[42] Navarro-Flores E, Chong Z, Omanovic S. Characterization of Ni, NiMo, NiW and NiFe electroactive coatings as electrocatalysts for hydrogen evolution in an acidic medium. J Mol Catal Chem 2005;226(2):179–97.
[43] Gao MY, Yang C, Zhang QB, Yu YW, Hua YX, Li Y, Dong P. Electrochemical fabrication of porous Ni-Cu alloy nanosheets with high catalytic activity for hydrogen evolution. Electrochim Acta 2016;215:609–16.